

Hardware realization of the multiply and accumulate operation on radio-frequency signals with magnetic tunnel junctions

Nathan Leroux¹, Alice Mizrahi^{1*}, Danijela Marković¹, Déaldo Sanz-Hernández¹, Juan Trastoy¹, Paolo Bortolotti¹, Leandro Martins², Alex Jenkins², Ricardo Ferreira², and Julie Grollier¹

¹Unité Mixte de Physique CNRS, Thales, Université Paris-Saclay, 91767 Palaiseau, France

²International Iberian Nanotechnology Laboratory (INL), 4715-31 Braga, Portugal

*alice.mizrahi@thalesgroup.com

Artificial neural networks are a valuable tool for radio-frequency (RF) signal classification in many applications, but digitization of analog signals and the use of general purpose hardware non-optimized for training make the process slow and energetically costly. Recent theoretical work has proposed to use nano-devices called magnetic tunnel junctions, which exhibit intrinsic RF dynamics, to implement in hardware the Multiply and Accumulate (MAC) operation – a key building block of neural networks – directly using analogue RF signals. In this article, we experimentally demonstrate that a magnetic tunnel junction can perform multiplication of RF powers, with tunable positive and negative synaptic weights. Using two magnetic tunnel junctions connected in series we demonstrate the MAC operation and use it for classification of RF signals. These results open the path to embedded systems capable of analyzing RF signals with neural networks directly after the antenna, at low power cost and high speed.

Introduction

Radio-frequency signals are widely used to convey information and there is an ever increasing demand for their accurate and quick analysis. Recently, artificial neural networks have proven successful for many RF processing applications such as signal classification¹, medical diagnosis^{2–4}, RF fingerprinting⁵, gesture sensing⁶, radar applications⁷ or aerial vehicle detection and identification⁸. Furthermore, they perform better than conventional algorithms, which rely on feature extractors and complex analysis tools, in terms of resilience to real-world conditions (noisy electromagnetic environment, imperfect RF components or antennas, etc.)¹. However, processing RF signals with neural networks requires analog signal digitization and training on CMOS-based hardware such as Graphical Processing Units, Tensor Processing Units or dedicated Application Specific Integrated Circuits. This process leads to millisecond delays and consumes hundreds of Watts, limiting the deployment of RF oriented artificial intelligence on embedded systems^{9,10}.

The need for compact and energy efficient RF hardware has stimulated research on emerging technologies which exhibit native RF dynamics. In particular, spintronic nano-oscillators can receive, transform and emit RF signals^{11–13}. They have been proposed as RF emitters and receivers for on-chip communication^{14–16} and can implement key operations for RF signal processing, such as spectral analysis^{17,18}. Furthermore, they are promising building blocks for neuromorphic computing^{19,20}. They have been implemented as neurons in feed-forward neural networks²¹, reservoir computing^{22–24} and synchronization-based computing^{25–27}. Recently, Leroux et al. ²⁸ have proposed using magnetic tunnel junctions as RF synapses to perform the Multiply and Accumulate (MAC) operation, i.e., a weighted sum in hardware, directly on analogue RF signals. The MAC operation is a key operation of neural networks, but it is particularly sensitive to the Von Neumann bottleneck because of the necessity to access memory for reading and writing the weights. Using emerging technologies to perform the MAC operation with collocation of memory and computing is thus projected to offer a hundred fold improvement in energy efficiency^{29–34}. Magnetic tunnel junctions can be scaled down to tens of

nanometers wide³⁵ and monolithically integrated into CMOS circuits³⁶. Thus, their use as RF synapses provides a path for compact, fast and energy efficient classification of RF signals. Leroux et al. used analytical work and numerical simulations to demonstrate that this MAC implementation could perform classification of handwritten digits images encoded into the RF signals powers²⁸.

In this work, we experimentally demonstrate that magnetic tunnel junctions can be used as RF synapses with tunable positive and negative weights. We further demonstrate experimentally the MAC operation on two RF inputs with two synapses, and use this MAC to perform 2D classification of RF signals.

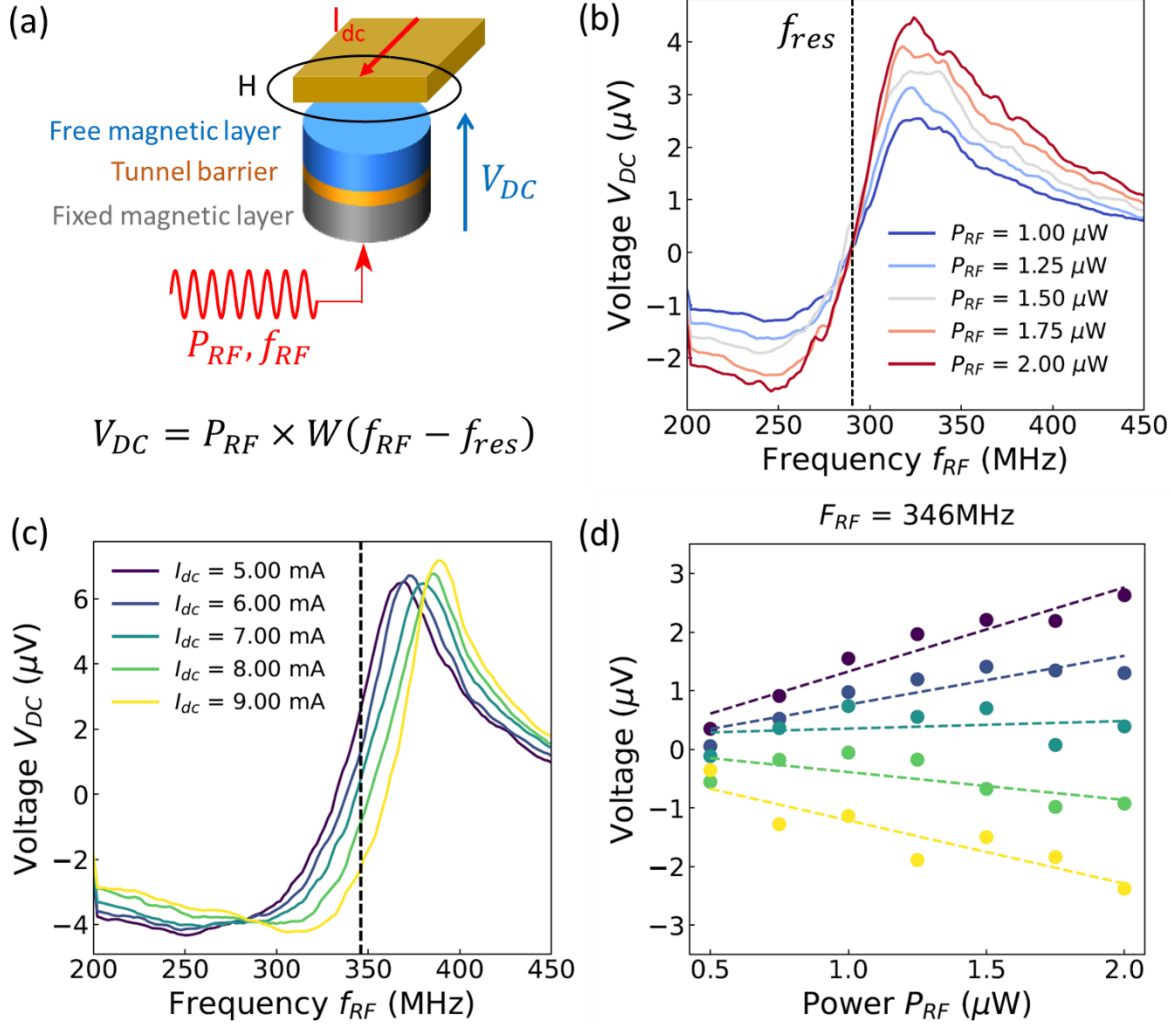


Figure 1 (a) Schematic of a magnetic tunnel junction performing a multiplication operation on an RF power P_{RF} . The synaptic weight is controlled through the resonance frequency f_{res} by application of a local magnetic field via direct current injection in a strip-line placed above the device. (b) Rectified dc voltage generated by the magnetic tunnel junction versus the frequency of the input RF signal, for various input powers. A vertical dashed line indicates the resonance frequency of the magnetic tunnel junction (c) Rectified dc voltage generated by the magnetic tunnel junction versus the frequency of the input RF signal, for an input power of 2 μW and for various dc currents applied in the strip line. The vertical dashed line marks the frequency 346 MHz. (d) Rectified dc voltage versus the input power for an input frequency of 346 MHz and for various dc currents applied in the strip line. All measurements were taken with a 6250 Oe perpendicular magnetic field applied to the device.

Methods: using a single magnetic tunnel junction as an RF synapse

We first demonstrate that a single magnetic tunnel junction can act as a synapse and multiply an RF power by a tunable weight, as schematized in Figure 1 (a). The device is a nanopillar magnetic tunnel junction stack of 250 nm diameter, made of SiO₂ // 5 Ta / 50 CuN / 5 Ta / 50 CuN / 5 Ta / 5 Ru / 6 IrMn / 2.0 Co₇₀Fe₃₀ / 0.7 Ru / 2.6 Co₄₀Fe₄₀B₂₀ / MgO / 2.0 Co₄₀Fe₄₀B₂₀ / 0.5 Ta / 7 NiFe / 10 Ta / 30 CuN / 7 Ru, where thickness are indicated in nm. It consists of a reference ferromagnetic layer (2.0 nm Co₄₀Fe₄₀B₂₀ / 0.5 nm Ta / 7 nm NiFe, where the CoFeB layer is there to ensure good crystallisation and is fully coupled to the NiFe layer such that they can be considered a single layer) pinned by a synthetic antiferromagnet structure, a tunnel barrier (MgO with RA of 8 Ohm μm^2) and a free magnetic layer (2.0 nm of CoFe₄₀B₂₀). The magnetization of the free layer is in a vortex state. When we inject an RF current through a magnetic tunnel junction, the core of the magnetic vortex in the free layer can be driven into gyrotropic motion, provided the input frequency is near the resonance frequency of the vortex. The tunnel magnetoresistance effect translates these magnetic oscillations into resistance oscillations. The mixing of the input RF current with the resistance oscillations at the same frequency give rise to a dc voltage across the junction, called spin-diode voltage^{12,37}. Figure 1 (b) presents this rectified voltage versus the input frequency f_{RF} . We observe a characteristic resonance curve around the resonance frequency (marked by a dashed vertical line). The amplitude of the voltage increases proportionally to the input power P_{RF} . By injecting a direct current in the strip-line placed above the device, we can create a local magnetic field collinear to the easy axis of the junction, as schematized in Figure 1 (a). This field modifies the resonance frequency of the vortex, as can be observed in Figure 1 (c), shifting the resonance curve. To demonstrate the synaptic operation, we fix the input frequency f_{RF} at 346 MHz (marked by a dashed vertical line in Figure 1 (c)), which is within the resonance window of the magnetic tunnel junction. Figure 1(d) presents the output voltage V_{DC} versus the input power P_{RF} , for various dc currents in the strip-line. We observe that the measured voltage (dots) shows a linear dependence (dashed lines) on the power P_{RF} , with the proportionality factor dependent on the dc tuning current, i.e. on the resonance frequency. As a consequence, the magnetic tunnel junction performs the operation:

$$V_{DC} = P_{RF} \times W$$

Where $W = W(f_{RF} - f_{res})$ is the synaptic weight, which is a function of the difference between the resonance frequency and the input frequency. Tuning the resonance frequency allows us to tune the synaptic weight. In order to successfully implement the synaptic operation, it is critical to be in the low power linear regime where the resonance frequency does not vary significantly with the input power, which is the case here. In future implementations, the tuning of the weight could be achieved in a non-volatile fashion by placing a memristive device on top of the free magnetic layer and electrically controlling its resonance frequency³⁸. Note that a single device is sufficient to implement both negative and positive values of the weight, which is an advantage over other synaptic nanodevices³⁰.

Results: Demonstration of the MAC operation with a synaptic chain

In order to demonstrate the MAC operation, we connect by wire bonding two magnetic tunnel junctions in series (MTJ 1 and MTJ 2), forming a synaptic chain, as schematized in Figure 2 (b). Figure 2 shows the characterization of the synaptic chain submitted to a single RF signal. In Figure 2 (a) we plot the voltage across the chain versus the input frequency f_{RF} and observe two resonance peaks, indicated by yellow and green zones, corresponding to MTJ 1 and MTJ 2 respectively. Figure 2 (c) and (d) show the effect of applying dc tuning currents I_1 and I_2 in the strip lines above MTJ 1 and MTJ 2 respectively. We observe that the resonance frequencies of both MTJs can be tuned within intervals larger than a hundred MHz. Figure 2 (e) and (f) show the voltage across the chain at fixed input

frequencies $f_{RF}^1 = 174$ MHz and $f_{RF}^2 = 540$ MHz respectively (dashed lines in Figure 2 (c) and (d) respectively) versus the input power, for different dc tuning currents. Fixing the frequency at $f_{RF}^1 = 174$ MHz (resp. $f_{RF}^2 = 540$ MHz) make it possible to address MTJ 1 (resp. MTJ 2). We observe that both MTJs perform the expected synaptic multiplication: the measured voltage (dots) can be described by a linear model (dashed lines). The synaptic weights W_1 and W_2 (slopes of the fits) are color encoded and depend on the tuning currents I_1 and I_2 .

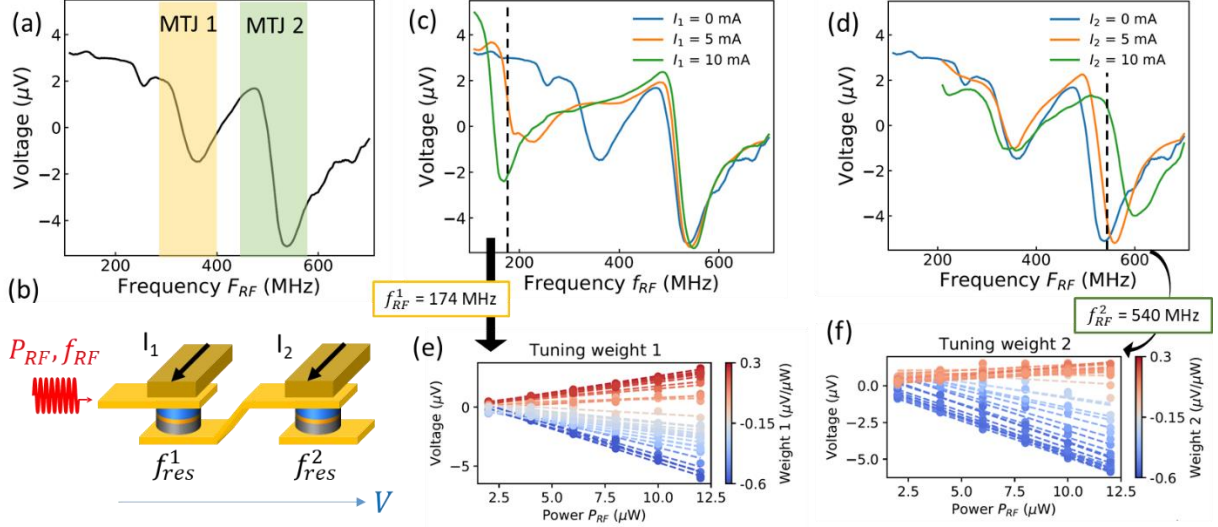


Figure 2 (a) Rectified dc voltage generated by the chain of two magnetic tunnel junctions versus the input frequency, for an input power of 12 μW . The yellow and green zones qualitatively indicate the frequency windows of MTJ 1 and MTJ 2 respectively. The voltage was smoothed with a moving average of ten points. (b) Schematic of the chain of two magnetic tunnel junctions submitted to an RF signal. (c-d) Rectified dc voltage versus the input frequency, for an input power of 12 μW , and for various values of I_1 while $I_2 = 0$ mA (c) and for various values of I_2 while $I_1 = 0$ mA (d). The vertical dashed lines mark the frequencies $f_{RF}^1 = 174$ MHz (c) and $f_{RF}^2 = 540$ MHz (d). (e-f) Rectified voltage versus input power, for an input frequency of $f_{RF}^1 = 174$ MHz (e) and $f_{RF}^2 = 540$ MHz (f), and for various tuning currents in the strip lines above both MTJs. The color bars in (e) and (f) indicate the synaptic weight associated to each MTJ. All measurements were taken with a 3500 Oe perpendicular magnetic field applied to the devices.

We now test the capability of this chain of two synapses to perform the MAC operation on two RF inputs. The inputs are two RF powers P_1 and P_2 , carried by signals at frequencies f_{RF}^1 and f_{RF}^2 respectively. We sum the two RF inputs using a power combiner and inject the resulting signal into the synaptic chain, as schematized in Figure 3 (a). We measure the output voltage generated by the chain for different combinations of P_1 , P_2 , W_1 and W_2 (i.e. for different combinations of P_1 , P_2 , I_1 and I_2). P_1 and P_2 were each varied from 2 to 12 μW by steps of 2 μW while I_1 and I_2 were each varied from 0 to 10 mA by steps of 2 mA. In Figure 3 (b) we compare the measured voltage across the chain for each combination (blue dots) to the ideally expected MAC voltage computed from single RF signal measurements (black line):

$$V_{MAC} = P_1 \times W_1 + P_2 \times W_2$$

with $W_1 = W_1(f_{RF}^1 - f_{res}^1)$ and $W_2 = W_2(f_{RF}^2 - f_{res}^2)$. For each combination of I_1 and I_2 , the values of W_1 and W_2 are extracted from the linear fits of the single RF signal input characterization (shown in Figure 2 (e) and (f)). We observe that the experimental voltage matches closely the ideal MAC voltage, with a slope of 0.99 and a root mean square error over all data points of 0.41 μV . In the next section, we evaluate the quality of this MAC operation by using it for RF signals classification then compare it to a simulated noisy MAC.

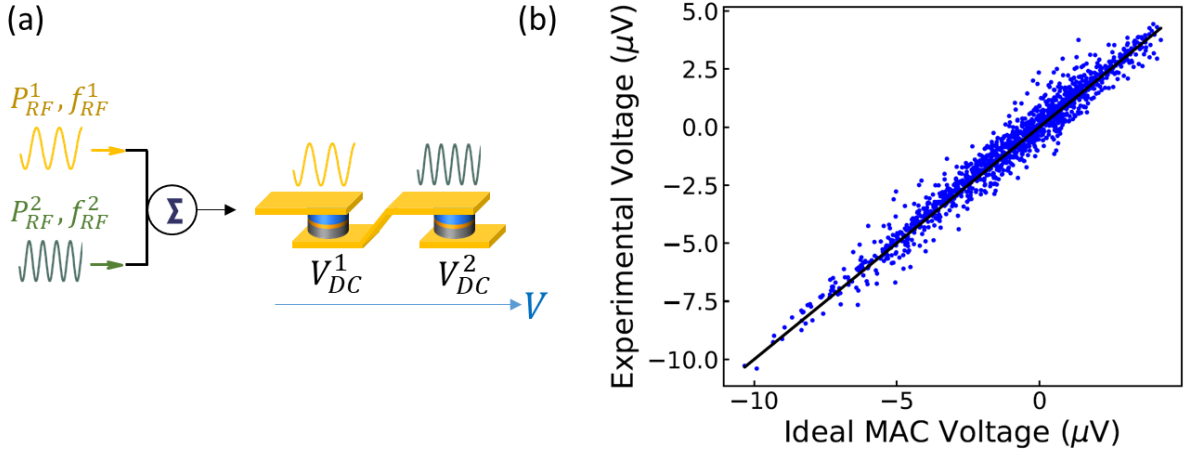


Figure 3 (a) Schematic of the MAC setup. (b) Measured rectified voltage (blue dots) and ideal MAC voltage (black line) versus the ideal MAC voltage. Each dot corresponds to a (P_1, P_2, W_1, W_2) configuration. All measurements were taken with a 3500 Oe perpendicular magnetic field applied to the devices.

Discussion: using the hardware RF MAC for RF signal classification

We illustrate the utility of this MAC operation by a simple classification example, shown in Figure 4 (a). The inputs are the powers P_1 and P_2 of RF signals at frequencies f_{RF}^1 and f_{RF}^2 . We apply a MAC operation to the inputs using the synaptic chain. If the measured output voltage is positive we classify the (P_1, P_2) input as “Class 1” (blue squares), while if the voltage is negative we classify the (P_1, P_2) input as “Class 0” (red dots). Each combination of weights defines a boundary in the 2D plane of axis P_1 and P_2 , and therefore constitutes a possible classification task. Here we first evaluate the classification accuracy for a classification task defined by a fixed predefined combination of weights. Figure 4 (b) shows the classification results for one classification task, corresponding to the following weight configuration: $W_1 = -0.50$ V/W and $W_2 = 0.23$ V/W (achieved by applying $I_1 = I_2 = 0$ mA). The dashed line is the boundary between the two classes expected from this weight configuration. The assigned classes are labeled by the blue squares and red dots. For this classification task, the experimental accuracy obtained – i.e. the proportion of correctly classified (P_1, P_2) inputs – is 100 %.

Figure 4 (c) shows the classification results for all configurations of fixed weights. Each black dot corresponds to a classification task defined by a weight configuration. The y-axis is the proportion of correctly classified (P_1, P_2) inputs while the x-axis is the root mean square error of the measured voltage compared to the ideal MAC voltage, computed over all (P_1, P_2) inputs. We observe that there is a correlation between classification accuracy and error on the MAC operation: a more precise MAC operation provides more accurate classification. However, we observe a large spread in classification accuracy for each average MAC error. Indeed, the classification accuracy is mainly set by the error brought by inputs close to the boundary (shown in black dashed line in Fig. 4b). This error is itself largely dependent on the values of P_1 and P_2 (larger powers tend to lead to larger errors). This dependency of errors on inputs explains the observed spread.

The mean accuracy averaged over all classification tasks (weight configurations) of our MAC operation is 93.9 %. In order to better evaluate the suitability of this accuracy, we perform the same classification with a simulated noisy MAC. We use the same inputs and weight configurations as for the experimental MAC. For each (P_1, P_2, W_1, W_2) configuration, we simulate the noisy MAC output by a voltage drawn from a normal distribution around the ideal MAC voltage. The standard deviation of the distribution is the mean square error obtained from the experiment for this weight configuration. The red crosses correspond to the classification results for the simulated noisy MAC. The overall accuracy for all the

weights configurations is 93.6 %. The fact that the experimental MAC and the simulated noisy MAC provide similar accuracies shows that the experimental MAC does not suffer from systematic errors and is indeed suitable for classification of RF signals.

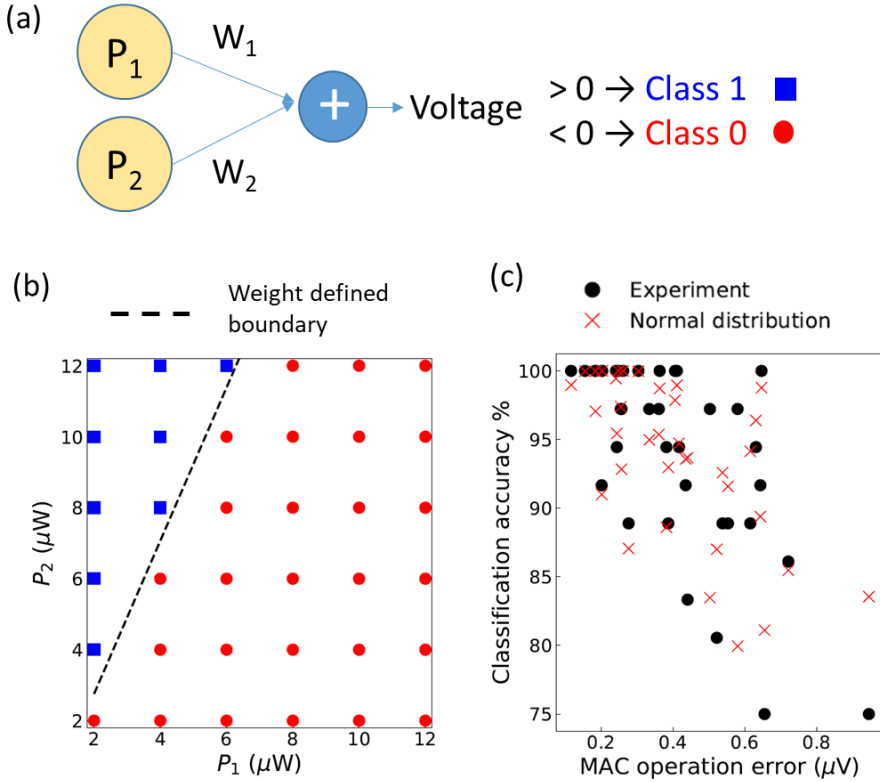


Figure 4 (a) Schematic of the performed 2D classification. A MAC operation with two weights is applied to input (P_1, P_2). A threshold is applied to the resulting voltage: values above 0 are classified as “Class 1” (blue squares) and values below zero as “Class 0” (red circles). (b) Classification results for all (P_1, P_2) inputs for one weight configuration: the dashed line represents the expected boundary between the classes 0 and 1, while the blue squares and red circles represent the class of each input as determined by the experimental voltage value. (c) Classification accuracy versus the error to the ideal MAC voltage. Each black circle corresponds to the accuracy of the experimental MAC for a given weight configuration (i.e. a target classification boundary). Each red cross corresponds to the accuracy of the simulated noisy MAC for a given weight configuration (same as the black circles). Each red cross accuracy is computed over all (P_1, P_2) inputs and average over 100 random trials for each input.

Conclusion

We have experimentally demonstrated that a magnetic tunnel junction can act as an RF synapse able to perform multiplication of RF powers on analogue RF signals, with tunable synaptic weights taking both positive and negative values. We have also demonstrated that several synapses in series can perform the multiply and accumulate operation, which is at the core of artificial neural networks. We illustrate the application of our system by performing a simple classification task on RF signals. This RF MAC implementation leverages the fact that each synapse is frequency selective, i.e. it only responds to RF signals in its resonance window. We expect this frequency multiplexing scheme to lead to the simplification of architecture for large neural networks, as a single signal combining all inputs can be sent to all synapses of a layer. These results were demonstrated here with vortex-state magnetic tunnel junctions, but could be applied to any spintronic resonator. In order to classify RF signals from various sources for applications, it is critical to have resonators responding to a wide range of frequencies. Vortex-state magnetic tunnel junctions can exhibit frequencies from tens of MHz to several GHz¹¹, and uniform mode magnetic tunnel junctions or spin Hall oscillators could act as synapses with frequencies up to tens of GHz^{26,40}. The same stack of materials can lead to resonators of

different frequencies, depending on the size and geometry of each device. Therefore, one could build an array of synapses of different resonance frequencies, able to respond to, and classify, RF signals over the 50 MHz – 50 GHz frequency range in parallel. Magneto-electrical effects can also be used to tune synaptic weights in a non-volatile fashion. This opens the path for compact, fast and energy efficient devices, allowing RF-signal classification in embedded systems.

Acknowledgements

This work is supported by the European Research Council ERC under Grant No. bioSPINspired 682955, the French ANR project SPIN-IA (Grant No. ANR-18-ASTR-0015), and the French Ministry of Defense (DGA).

References

1. O’Shea, T. J., Roy, T. & Clancy, T. C. Over-the-Air Deep Learning Based Radio Signal Classification. *IEEE J. Sel. Top. Signal Process.* **12**, 168–179 (2018).
2. Yoon, Y. H., Khan, S., Huh, J. & Ye, J. C. Efficient B-Mode Ultrasound Image Reconstruction From Sub-Sampled RF Data Using Deep Learning. *IEEE Trans. Med. Imaging* **38**, 325–336 (2019).
3. Dai, M., Li, S., Wang, Y., Zhang, Q. & Yu, J. Post-processing radio-frequency signal based on deep learning method for ultrasonic microbubble imaging. *Biomed. Eng. OnLine* **18**, 95 (2019).
4. Besler, E., Wang, Y. C. & Sahakian, A. V. Real-Time Radiofrequency Ablation Lesion Depth Estimation Using Multi-frequency Impedance With a Deep Neural Network and Tree-Based Ensembles. *IEEE Trans. Biomed. Eng.* **67**, 1890–1899 (2020).
5. Merchant, K., Revay, S., Stantchev, G. & Nousain, B. Deep Learning for RF Device Fingerprinting in Cognitive Communication Networks. *IEEE J. Sel. Top. Signal Process.* **12**, 160–167 (2018).
6. Lien, J. *et al.* Soli: ubiquitous gesture sensing with millimeter wave radar. *ACM Trans. Graph.* **35**, 142:1-142:19 (2016).

7. Kim, Y. Application of Machine Learning to Antenna Design and Radar Signal Processing: A Review. in *2018 International Symposium on Antennas and Propagation (ISAP)* 1–2 (2018).
8. Al-Sa'd, M. F., Al-Ali, A., Mohamed, A., Khattab, T. & Erbad, A. RF-based drone detection and identification using deep learning approaches: An initiative towards a large open source drone database. *Future Gener. Comput. Syst.* **100**, 86–97 (2019).
9. García-Martín, E., Rodrigues, C. F., Riley, G. & Grahn, H. Estimation of energy consumption in machine learning. *J. Parallel Distrib. Comput.* **134**, 75–88 (2019).
10. Big data needs a hardware revolution. *Nature* **554**, 145–146 (2018).
11. Dussaux, A. *et al.* Large microwave generation from current-driven magnetic vortex oscillators in magnetic tunnel junctions. *Nat. Commun.* **1**, 8 (2010).
12. Tulapurkar, A. A. *et al.* Spin-torque diode effect in magnetic tunnel junctions. *Nature* **438**, 339–342 (2005).
13. Fang, B. *et al.* Experimental Demonstration of Spintronic Broadband Microwave Detectors and Their Capability for Powering Nanodevices. *Phys. Rev. Appl.* **11**, 014022 (2019).
14. Choi, H. S. *et al.* Spin nano–oscillator–based wireless communication. *Sci. Rep.* **4**, 5486 (2014).
15. Ruiz-Calaforra, A. *et al.* Frequency shift keying by current modulation in a MTJ-based STNO with high data rate. *Appl. Phys. Lett.* **111**, 082401 (2017).
16. Marković, D. *et al.* Detection of the Microwave Emission from a Spin-Torque Oscillator by a Spin Diode. *Phys. Rev. Appl.* **13**, 044050 (2020).
17. Litvinenko, A. *et al.* Ultrafast Sweep-Tuned Spectrum Analyzer with Temporal Resolution Based on a Spin-Torque Nano-Oscillator. *Nano Lett.* **20**, 6104–6111 (2020).
18. Menshawy, S. *et al.* Spin transfer driven resonant expulsion of a magnetic vortex core for efficient rf detector. *AIP Adv.* **7**, 056608 (2016).
19. Grollier, J. *et al.* Neuromorphic spintronics. *Nat. Electron.* **3**, 360–370 (2020).
20. Marković, D., Mizrahi, A., Querlioz, D. & Grollier, J. Physics for neuromorphic computing. *Nat. Rev. Phys.* **2**, 499–510 (2020).

21. Cai, J. *et al.* Sparse neuromorphic computing based on spin-torque diodes. *Appl. Phys. Lett.* **114**, 192402 (2019).
22. Marković, D. *et al.* Reservoir computing with the frequency, phase, and amplitude of spin-torque nano-oscillators. *Appl. Phys. Lett.* **114**, 012409 (2019).
23. Torrejon, J. *et al.* Neuromorphic computing with nanoscale spintronic oscillators. *Nature* **547**, 428–431 (2017).
24. Tsunigi, S. *et al.* Physical reservoir computing based on spin torque oscillator with forced synchronization. *Appl. Phys. Lett.* **114**, 164101 (2019).
25. Romera, M. *et al.* Vowel recognition with four coupled spin-torque nano-oscillators. *Nature* **563**, 230–234 (2018).
26. Zahedinejad, M. *et al.* Two-dimensional mutually synchronized spin Hall nano-oscillator arrays for neuromorphic computing. *Nat. Nanotechnol.* **15**, 47–52 (2020).
27. Koo, M. *et al.* Distance Computation Based on Coupled Spin-Torque Oscillators: Application to Image Processing. *Phys. Rev. Appl.* **14**, 034001 (2020).
28. Leroux, N. *et al.* Radio-Frequency Multiply-And-Accumulate Operations with Spintronic Synapses. *ArXiv201107885 Cond-Mat* (2020).
29. Cai, F. *et al.* A fully integrated reprogrammable memristor–CMOS system for efficient multiply–accumulate operations. *Nat. Electron.* **2**, 290–299 (2019).
30. Yao, P. *et al.* Fully hardware-implemented memristor convolutional neural network. *Nature* **577**, 641–646 (2020).
31. Ambrogio, S. *et al.* Equivalent-accuracy accelerated neural-network training using analogue memory. *Nature* **558**, 60–67 (2018).
32. Xu, X. *et al.* 11 TOPS photonic convolutional accelerator for optical neural networks. *Nature* **589**, 44–51 (2021).
33. Hamerly, R., Bernstein, L., Sludds, A., Soljačić, M. & Englund, D. Large-Scale Optical Neural Networks Based on Photoelectric Multiplication. *Phys. Rev. X* **9**, 021032 (2019).

34. Xue, C.-X. *et al.* A CMOS-integrated compute-in-memory macro based on resistive random-access memory for AI edge devices. *Nat. Electron.* **4**, 81–90 (2021).
35. Sato, H. *et al.* Properties of magnetic tunnel junctions with a MgO/CoFeB/Ta/CoFeB/MgO recording structure down to junction diameter of 11 nm. *Appl. Phys. Lett.* **105**, 062403 (2014).
36. Golonzka, O. *et al.* MRAM as Embedded Non-Volatile Memory Solution for 22FFL FinFET Technology. in *2018 IEEE International Electron Devices Meeting (IEDM)* 18.1.1-18.1.4 (2018). doi:10.1109/IEDM.2018.8614620.
37. Fang, B. *et al.* Giant spin-torque diode sensitivity in the absence of bias magnetic field. *Nat. Commun.* **7**, 11259 (2016).
38. Zahedinejad, M. *et al.* Memristive control of mutual SHNO synchronization for neuromorphic computing. *ArXiv200906594 Phys.* (2020).
39. Grollier, J. Chaîne synaptique comprenant des résonateurs spintroniques basés sur l'effet de diode de spin et réseau de neurones comprenant une telle chaîne synaptique. (2020).
40. Bonetti, S., Muduli, P., Mancoff, F. & Åkerman, J. Spin torque oscillator frequency versus magnetic field angle: The prospect of operation beyond 65 GHz. *Appl. Phys. Lett.* **94**, 102507 (2009).